



Ultrasonic vibration-assisted joining of multiform metallic glasses in varied environments

Lu-Yao Li, Jian-Yu Chen, Li-Xing Zhu, Yu Zhang, Jian Zhu, Xin Li, Wei Li, Kang-Yu Lin, Xing-Ran Zhao, Xiao-Di Liu, Chen-Chen Yuan*, Jiang Ma*

Received: 24 June 2025 / Revised: 1 August 2025 / Accepted: 5 August 2025
© Youke Publishing Co., Ltd. 2025

Abstract The evolution of joining technologies has profoundly propelled advancements across human civilization. Although modern joining processes have attained remarkable sophistication in conventional manufacturing, construction, and aerospace applications, their operational adaptability in special environments—including underwater, hyper-corrosive, explosive, and cryogenic conditions—remains fundamentally constrained. This limitation underscores the critical demand for facile and robust joining methodologies tailored for specialized environments. Here, we present an innovative strategy using ultrasonic vibration to enable joining across diverse metallic glasses morphologies under these demanding conditions. Leveraging

ultrasonic vibration-induced plasticity and the unique activation mechanisms of metallic glasses, this approach demonstrates unprecedented compatibility with bulk, ribbon, and powder forms. Distinct engineered joint structures emerge across different materials, achieving mechanical strengths comparable to parent materials (1904 MPa compressive strength). This breakthrough establishes a transformative platform for offshore, polar, oil–gas, and space engineering applications and pioneers a universal design way for materials with programmable performance characteristics.

Keywords Varied environments; Joining; Metallic glasses; Ultrasonic Vibration

Supplementary Information The online version contains supplementary material available at <https://doi.org/10.1007/s12598-025-03603-5>.

L.-Y. Li, W. Li, C.-C. Yuan*
School of Materials Science and Engineering, Jiangsu Key Laboratory for Advanced Metallic Materials, Southeast University, Nanjing 211189, China
e-mail: yuanchenchenneu@hotmail.com

L.-Y. Li, J.-Y. Chen, L.-X. Zhu, Y. Zhang, J. Zhu, X. Li, K.-Y. Lin, X.-R. Zhao, X.-D. Liu, J. Ma*
Shenzhen Key Laboratory of High Performance Nontraditional Manufacturing, College of Mechatronics and Control Engineering, Shenzhen University, Shenzhen 518060, China
e-mail: majiang@szu.edu.cn

J. Ma
Guangdong Provincial Key Laboratory of Micro/Nano Optomechatronics Engineering, Shenzhen University, Shenzhen 518060, China

J. Ma
State Key Laboratory of Radio Frequency Heterogeneous Integration, Shenzhen University, Shenzhen 518060, China

1 Introduction

Joining technology has served as a cornerstone in the advancement of human civilization, evolving into a pivotal manufacturing discipline in contemporary industry [1, 2]. The most representative joining techniques are a series of welding techniques, including laser welding, arc welding, high-temperature brazing, electron beam welding, resistance welding, and friction welding [3]. Emerging technologies like powder metallurgy [4, 5] and additive manufacturing (3D printing) [6] have demonstrated breakthrough advancements in precision-driven domains, including microelectronics and high-accuracy fabrication systems [7]. Nowadays, the environment of the joining process exhibits a diversifying trend. For instance, with the vigorous development of marine engineering recently, including in the field of shipbuilding, offshore oil and gas development, and the construction of ocean platforms, underwater joining technology has become a critical



component to be used in manufacturing and repairing [8, 9]. Furthermore, safety-critical maintenance operations for energy storage containers handling flammable substances like petroleum, natural gas, and organic solvents, as well as their associated transportation pipeline, demand specialized joining solutions [10, 11]. The most technologically challenging environment involves cryogenic conditions that dominate cosmic scales [12], encompassing strategically significant regions such as Earth's polar zones, space station orbital environments, and extraterrestrial surfaces like the Moon and Martian terrain [13].

When facing the above extreme environments, most techniques are unusable, because of the catastrophic risks associated with electrical arcs and elevated thermal inputs [14]. Currently, only underwater welding is a relatively mature technique [8], which is generally divided into dry welding [15] and wet welding [16]. Dry welding employs specialized pressure-resistant enclosures to mitigate rapid heat dissipation and hydrostatic effects, while wet welding demonstrates superior operational flexibility through direct aqueous implementation [17, 18], enabling its widespread adoption in marine engineering applications [16]. Nevertheless, three critical limitations persist in wet welding methodologies: (1) the metastable molten pool undergoes ultra-rapid solidification under aqueous quenching, notably degrading mechanical strength through hardened microstructures [9, 19]; (2) endogenous gas evolution from water dissociation generates porosity clusters containing hydrogen and oxygen byproducts [20, 21]; (3) the requisite high-amperage currents (500-800A) for metal liquefaction introduce substantial electrical hazards to personnel [22]. These inherent constraints significantly restrict its application spectrum in special environments. Furthermore, welded joints are inevitably susceptible to mechanical property deterioration and corrosion resistance degradation when exposed to special service environments [23] prevalent in defense systems, deep-sea mining infrastructure, energy storage facilities, and space exploration applications. These demanding scenarios necessitate exceptional resistance to synergistic environmental challenges such as deep-sea pressure fluctuations, erosion, space radiation bombardment, and cyclical thermal stress loading [24]. However, current welding materials exhibit inherent limitations in achieving concurrent optimization of these special service properties [10, 25]. This critical challenge underscores the imperative for developing innovative joining technologies and advanced materials engineering strategies to fulfill the escalating performance demands in next-generation joining processes.

Metallic glasses (MGs) have gained prominence, exhibiting remarkable adaptability to extreme environments, primarily attributed to their unique amorphous atomic configuration that circumvents crystalline lattice limitations

[26–28]. These materials demonstrate an exceptional combination of mechanical and functional characteristics, including ultrahigh strength [29], superior elastic strain limit [30], outstanding wear resistance [31], radiation tolerance [32], thermal cycling stability [33], and exceptional corrosion resistance [34], positioning them as pivotal candidates for mission-critical applications in aerospace and marine engineering domains. Nevertheless, two fundamental challenges persist in their technological advancement: the intrinsic restriction of glass-forming ability (GFA) that impedes bulk-scale fabrication [35] and poses challenges in processing due to the paradoxical combination of extreme mechanical strength with crystallization susceptibility [36]. While extensive research has focused on GFA enhancement through compositional engineering [37–39], transformative breakthroughs remain elusive. Joining technology emerges as a dual-purpose solution addressing both bulk fabrication scalability and component processability [40–42], with current methodologies predominantly following two mechanistic pathways. The first category employs rapid melting-solidification cycles through techniques like laser welding [43], explosive welding [44], and electro-pulse welding [45], while the second leverages viscous flow behavior in the supercooled liquid region via thermoplastic bonding [40, 41] or friction stir welding [46]. Both approaches, however, suffer from inherent constraints, including excessive thermal input, time consumption characteristics, and equipment complexity that limit deployment in operational harsh environments. Recent discovery of a non-thermal ultrasonic vibration mechanism [47, 48] introduces a paradigm shift by enabling millisecond-scale liquid-like MG behavior through athermal activation, thereby establishing an innovative platform for material processing. Building on this principle, researcher successfully achieves ultrasonic vibration welding of MGs in an ambient atmosphere [49–51]. This breakthrough methodology synergistically addresses both environmental compatibility limitations, opening new frontiers for joining in special service conditions.

Based on the synergistic integration of advanced materials and innovative technology, this study presents a universal ultrasonic vibration joining (UVJ) method engineered for extreme operational conditions. To validate its adaptability, UVJ processes were implemented under simulated special environments including pure water (marine applications), citric acid solutions (highly corrosive scenarios), anhydrous ethanol (flammable/explosive contexts), and liquid nitrogen ($-196\text{ }^{\circ}\text{C}$, polar/space environments), demonstrating successful bonding across diverse material systems encompassing metallic glasses (MGs) in bulk, ribbon, and powder morphologies. During joining, dynamic heterogeneity and liquid-like behavior under ultrasonic vibration facilitate oxide layer disruption and metallic bonding, with distinct fluid dynamics and

oxide fragmentation stages observed across morphologies, thereby yielding tailored joint structures. The resulting joints exhibit mechanical strength comparable to cast MGs (1904 MPa). This breakthrough establishes UVJ as a versatile platform technology for special-environment engineering applications spanning offshore, polar, oil–gas, and aerospace sectors, while proposing a paradigm for designing composites with programmable properties through flexible process–material interplay.

2 Experimental

2.1 Raw material preparation

The present study selected Zr-based ($\text{Zr}_{55}\text{Cu}_{30}\text{Al}_{10}\text{Ni}_5$) and TiZrHfBeNi high-entropy metallic glasses (HE-MGs) as the primary connecting materials for MGs. High-purity elemental metals were arc-melted and cast into bulk specimens using water-cooled copper molds under a low-pressure argon atmosphere (0.05 MPa). Cylindrical rods with a diameter of 5 mm and rectangular plates featuring a cross-section of 1 mm × 10 mm were fabricated as the primary bulk material forms. MG ribbons were fabricated via vacuum arc melting followed by rapid solidification through single-wheel melt-spinning. These ribbons were subsequently mechanically fragmented into segments measuring 2–5 mm in length using precision shears. MG powders were synthesized by vacuum arc melting and high-pressure gas atomization (argon: 4.0 MPa), yielding particles with a controlled size distribution of 15–53 μm . The Pure monomers used were listed as follows: Zr (99.95%), Al (99.99%), Ni (99.98%), Cu (99.95%), Hf (99.95%), Ti (99.995%), and Be (99.9%).

2.2 Joining environments

This study established an environmental simulation framework: (1) water were employed to replicate ubiquitous hydrospheric environments such as lakes and oceans; (2) anhydrous ethanol ($\geq 99.7\%$) served as a representative medium for simulating combustion-prone organic solvents and liquid fuels; (3) a 10% (w/v) citric acid monohydrate solution ($\text{Ph} \approx 1.7 \pm 0.2$) was formulated to mimic corrosive environments; and (4) cryogenic exposure was implemented using liquid nitrogen (boiling point: $-196\text{ }^\circ\text{C}$) to simulate extreme low-temperature environment.

2.3 Ultrasonic vibration joining process

The ultrasonic vibration systems consist of an ultrasonic generator (emitting electrical signals), and a transducer (converting electrical signals into vibration signals), a

booster (amplifying the amplitude of the vibration signals) and ultimately outputting high-frequency vibrations under certain pressure by a sonotrode, as shown in Fig. S1. The ultrasonic sonotrode was pneumatically driven at 350 kPa to apply pressure perpendicular to the contact surface. Upon detecting a force threshold of $200 \pm 1\text{ N}$ via a piezoelectric force sensor, ultrasonic vibration was immediately initiated. The vibration frequency is 20,000 Hz ($\pm 500\text{ Hz}$), with an amplitude of 44.4 μm ($\pm 1\text{ }\mu\text{m}$). To further investigate the UVJ process, a homemade force sensor and a data acquisition card with a sampling frequency of 1 kHz (National Instruments NI-9237) were used to measure the pressure and transmit the data to a computer. Simultaneously, a K-type thermocouple and a data acquisition card (sampling frequency of 100 Hz) were used to measure the real-time temperature of powders, ribbons, and bulk materials, with a measurement accuracy of 0.2 $^\circ\text{C}$. Special measurement methods were employed for precise measurement of the temperature at the joining process, as shown in Fig. S2. The high-speed camera (Revealer X50) was used to capture the joining process of bulk MGs.

2.4 Mechanical properties test

The hardness test was performed on MGs and composites using a Vickers hardness tester under a load of 500 gf (4.90 N) and held for 10 s. To perform compression testing, the samples were cut into standard cylinder specimens with a length/diameter ratio of 1.5 (length of 2.25 mm and diameter of 1.5 mm). The compress testing with an initial strain rate of 0.001 s^{-1} was performed on a universal testing machine (Z050TEW) at room temperature. The hardness and modulus of the sample surfaces were measured by the Berkovich triangular pyramid indenter with a maximum load of 8 mN and constant loading rates of 5 mN s^{-1} , then held the load for 10 s.

2.5 Multi-scale structural characterizations

The structural properties of all the samples in the present research were ascertained by XRD (Rigaku MiniFlex 600) with Cu $K\alpha$ radiation at a scanning rate of 5° min^{-1} from 20° to 80° . The micromorphologies and elemental distributions of samples were characterized by an FEI Quanta 450 FEG field emission scanning electron microscope (SEM) instrument equipped with energy-dispersive X-ray spectroscopy (EDS). The nanoscale morphologies and structural properties were characterized using a transmission electron microscope (TEM, Fei Titan Themis) equipped with EDS. The TEM samples were prepared on a FEI Scios SEM/FIB dual-beam system. Due to the inability of EDS to precisely detect Be and interference from the Cu

semi-ring support in the TEM sample holder on Cu signals, both Cu and Be elements were excluded from the EDS analysis. The three-dimensional perspective scanning of the joined MGs was performed by the computed tomography (CT, Sanying precision instruments-nano Voxel 3000d) device, which was conducted at a voxel size of $3\ \mu\text{m} \times 3\ \mu\text{m} \times 3\ \mu\text{m}$. The dynamic scanning probe microscopy (DSPM) was detected by two characterization techniques. The nanodynamic mechanical analysis (nano-DMA) mode in the nanoindenter (TI950, Hysitron) was conducted with a tip frequency of 200 Hz and a pressure of 6 μN . The amplitude modulation-frequency modulation (AM-FM) viscoelastic mapping mode in atomic force microscopy (AFM, Oxford Instrument) was performed with a frequency of 72,000 Hz and 142,000 Hz. To minimize the influence of surface roughness on experimental results, all DSPM tests were conducted on $\text{Zr}_{55}\text{Cu}_{30}\text{Al}_{10}\text{Ni}_5$ MG-coated samples.

3 Results and discussion

3.1 Joining process

Figure 1A schematically illustrates the UVJ system designed for special environments, which comprises an integrated ultrasonic generator and a precision mechanical vibration apparatus. To validate the system's adaptability, three distinct material morphologies (bulk, ribbon, and powder forms) were systematically processed in four representative media: water, organic solvents (anhydrous ethanol), acidic environments (10% citric acid), and cryogenic conditions (liquid nitrogen immersion). Figure 1B demonstrates the methods for bonding across these material-environment combinations. Post-joining analysis revealed that all configurations achieved exceptional interfacial integrity while retaining their inherent metallic luster, confirming the process's efficacy under special conditions. The samples obtained in all environments are shown in Fig. S3, in which similar joining quality was achieved.

The pressure evolution during ultrasonic vibration joining (UVJ) processing was quantitatively monitored using a custom-developed real-time pressure acquisition system. Experimental data revealed that under optimized joining conditions, the powder specimen exhibited the highest interfacial pressure, followed by the ribbon and bulk material configurations (Fig. 1C). This pressure hierarchy can be attributed to the extended dwell time required for powder systems to achieve adequate densification within the ultrasonic vibration field. To elucidate the thermodynamic characteristics governing UVJ mechanisms, synchronized temperature profiling was conducted

via a K-type thermocouple. All material systems exhibited negligible thermal effects in water environments, with transient temperature spikes below 100 °C persisting for merely 0.01–0.02 s per acquisition cycle. The maximum recorded temperatures for bulk, ribbon, and powder specimens measured 90.1, 60.1, and 59.1 °C, respectively (Fig. 1D), demonstrating 1–2 orders of magnitude lower thermal input compared to conventional fusion welding. Temperature measurements in alcohol and liquid nitrogen indicated that the temperature rise remained minimal (Fig. S3), further substantiating the predominance of non-thermal effects in the joining process. The synergistic analysis of pressure–temperature metrics conclusively establishes UVJ as a solid-state joining mechanism fundamentally distinct from melt-dominated processes. This mechanism was corroborated by high-speed imaging, capturing the sequential interfacial softening of metallic glasses and subsequent metallurgical bond formation in bulk materials (Fig. 1E; Movie S1). Significantly, this process aligns with the joining behavior of MGs in ambient air, see Movie S2.

3.2 The multi-joining under special environments

The applicability of advanced joining technologies is fundamentally determined by their capacity to process materials with divergent morphologies and heterogeneous compositions. To rigorously evaluate the UVJ methodology in special environments, the technology's performance was systematically assessed using three representative material forms: bulk, ribbon, and powder specimens. This dual capability in material form adaptability (solid-state to particulate) and heterogeneous join compatibility establishes UVJ as a universal joining platform, particularly advantageous for special-environment applications where conventional fusion-based techniques prove inadequate.

The systematic evaluation of interfacial integrity in bulk materials processed by UVJ is presented in Fig. 2. X-ray computed tomography (CT) was employed to comparatively analyze homogeneous ($\text{Zr}_{55}\text{Cu}_{30}\text{Al}_{10}\text{Ni}_5$ MG) and heterogeneous (TiZrHfBeNi MG/ $\text{Zr}_{55}\text{Cu}_{30}\text{Al}_{10}\text{Ni}_5$ MG) joints (Fig. 2A, B), with comprehensive pictures provided in Fig. S4. Six cutting positions reveal seamless bonding interfaces in both configurations, as evidenced by uniform and continuous density gradients at the joint regions (color-mapped below CT images). The heterogeneous interface exhibits characteristic fractal-like morphology (Fig. 2B, green: TiZrHfBeNi MG; blue: $\text{Zr}_{55}\text{Cu}_{30}\text{Al}_{10}\text{Ni}_5$ MG). This morphological signature provides evidence of the non-Newtonian fluidic behavior of MGs during UVJ, where localized viscoelastic flow enables atomic interdiffusion without bulk crystallization. The absence of interfacial voids or cracks at macroscopic scales confirms the

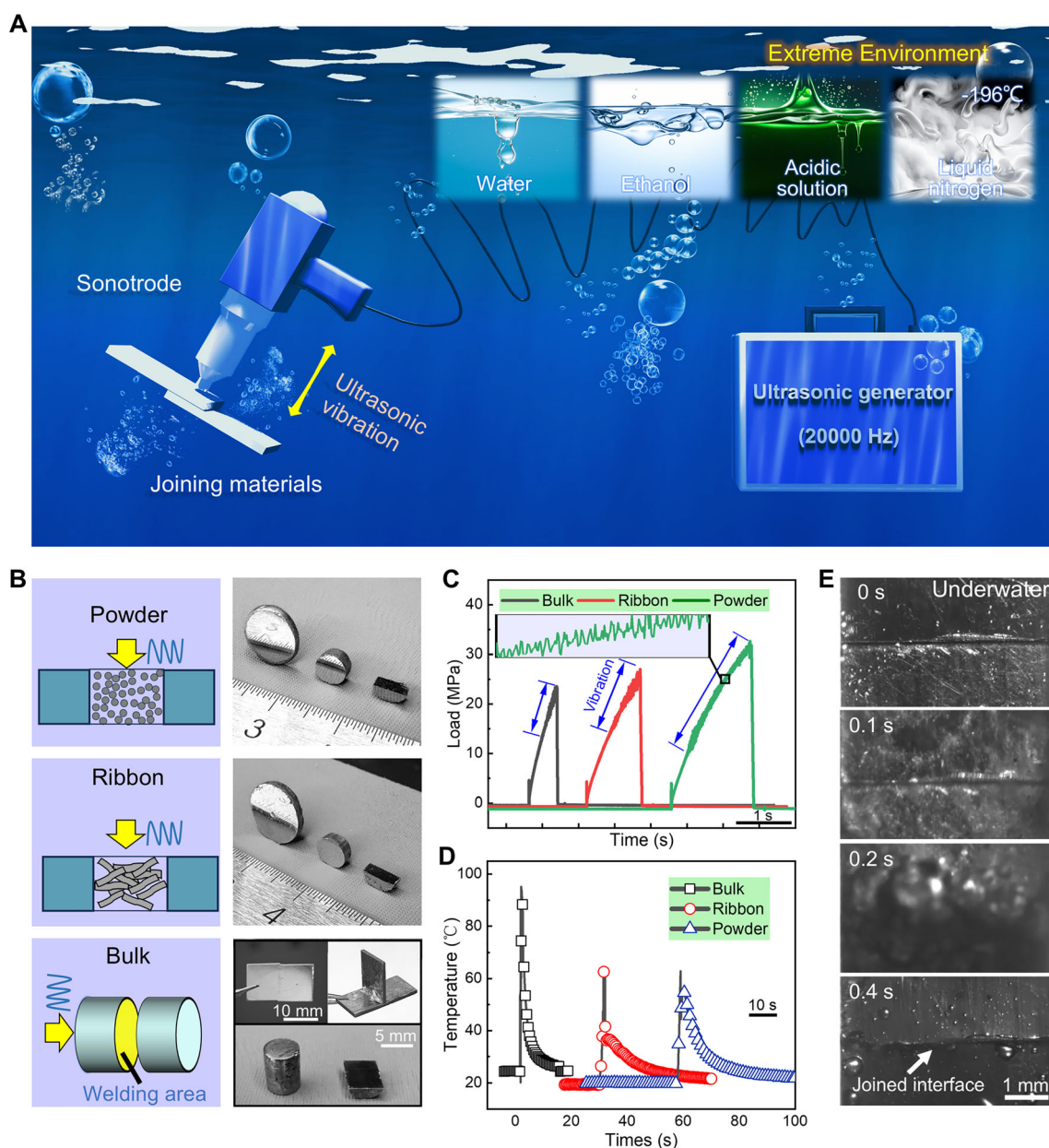


Fig. 1 The display of joining processes. **A** Schematic diagram of joining under special environments. **B** Samples display diagrams of underwater joined samples with 3 different morphologies of MGs (powder, ribbon, bulk). **C** Stress-time curve of joining in 3 different morphologies of MGs. **D** Temperature–time curve of 3 different morphologies of MGs join, which was measured under water. **E** Joining process under water was captured by a high-speed camera

process's effectiveness in achieving metallurgical continuity across dissimilar MG systems.

The interfacial integrity and microstructure of joined bulk MGs were analyzed to evaluate the joining efficacy. Field emission scanning electron microscopy (FE-SEM) was used to reveal defect-free interfaces throughout the TiZrHfBeNi MG/Zr₅₅Cu₃₀Al₁₀Ni₅ MG joint (Fig. 2C), while X-ray diffraction (XRD) confirmed the preserved amorphous structure without crystallization signatures (Fig. 2D). Complementing computed tomography

observations, FE-SEM imaging exposed fractal-like interfacial morphology where two distinct amorphous phases exhibited interpenetration zones spanning several micrometers. Energy-dispersive X-ray spectroscopy (EDS) elemental mapping at enhanced resolutions demonstrated progressive intermixing across the interface, evidenced by transitional gradients in elemental distributions (Fig. 2E). The joining effect between Zr₅₅Cu₃₀Al₁₀Ni₅ MG/Zr₃₅Ti₃₀Be_{26.75}Cu_{8.25} MG was similar to the former, achieving seamless joining throughout the entire sample

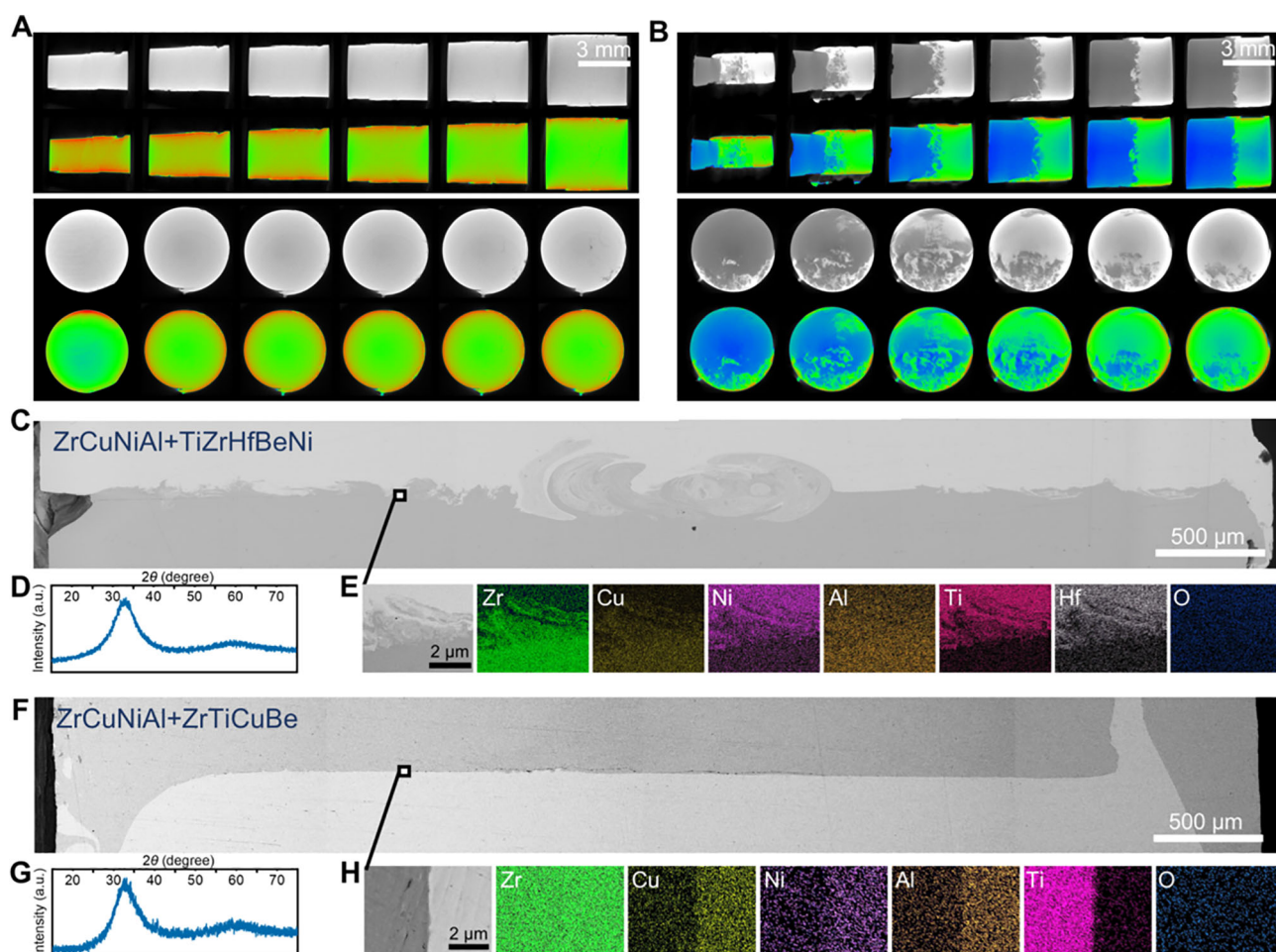


Fig. 2 Bonding quality characterization of the bulk-joined sample. **A, B** CT scan patterns and the corresponding density distribution of homogeneous ($Zr_{55}Cu_{30}Al_{10}Ni_5$ MG) and heterogeneous ($Zr_{55}Cu_{30}Al_{10}Ni_5$ MG/ $TiZrHfBeNi$ MG) joined samples. The scanning direction is the longitudinal section and the cross-section. **C** Field emission SEM images of the $Zr_{55}Cu_{30}Al_{10}Ni_5$ MG/ $TiZrHfBeNi$ MG joined sample. **D** XRD patterns of the $Zr_{55}Cu_{30}Al_{10}Ni_5$ MG/ $TiZrHfBeNi$ MG joined sample. **E** SEM image of the joined interface and corresponding EDS image. **F–H** SEM image, XRD, and corresponding EDS images of the $Zr_{35}Ti_{30}Be_{26.75}Cu_{8.25}$ MG/ $Zr_{55}Cu_{30}Al_{10}Ni_5$ MG joined sample

range while still maintaining an amorphous state (Fig. 2F–H).

The bonding quality characterization of the joined ribbon raw materials is shown in Fig. 3A–H. Both homogeneous ($Zr_{55}Cu_{30}Al_{10}Ni_5$ MG) and heterogeneous ($TiZrHfBeNi$ MG/ $Zr_{55}Cu_{30}Al_{10}Ni_5$ MG) joints exhibit defect-free interfaces in the reconstructed CT images and corresponding density profiles (Fig. 3A, B). Notably, the heterogeneous joint reveals a distinct lamellar architecture post-bonding, with alternating amorphous layers maintaining structural integrity; this structure is attributed to the ribbon stacking during joining (Fig. 3E; detailed visualization in Fig. S5). Furthermore, higher magnification shows that both homogeneous (Fig. 3D, E) and heterogeneous (Fig. 3G, H) joints achieve defect-free metallurgical bonding at the microscopic scale while retaining full amorphous characteristics (Fig. 3C, F) and preventing

crystallization. Notably, and conversely to the behavior observed in bulk joints (Fig. 2C–E), the ribbon joints display a fundamentally distinct interfacial behavior (Fig. 3F–H), exhibiting clear phase boundaries without significant interface mixing zones.

The bonding characteristics of powder materials in subaqueous environments are systematically illustrated in Fig. 3I–P. Despite conventional wisdom suggesting that surface oxides significantly impede powder joining [41, 52], CT analysis reveals exceptional defect-free interfaces in both homogeneous and heterogeneous powder-bonded systems (Fig. 3I, J; detailed visualization in Fig. S6). Macroscopically, both join types lack significant voids and maintain perfect amorphous structures (Fig. 3K, N), with the heterogeneous joint revealing a well-defined biphasic architecture featuring uniform phase distribution. At the microscopic scale, homogeneous systems (pure Zr-

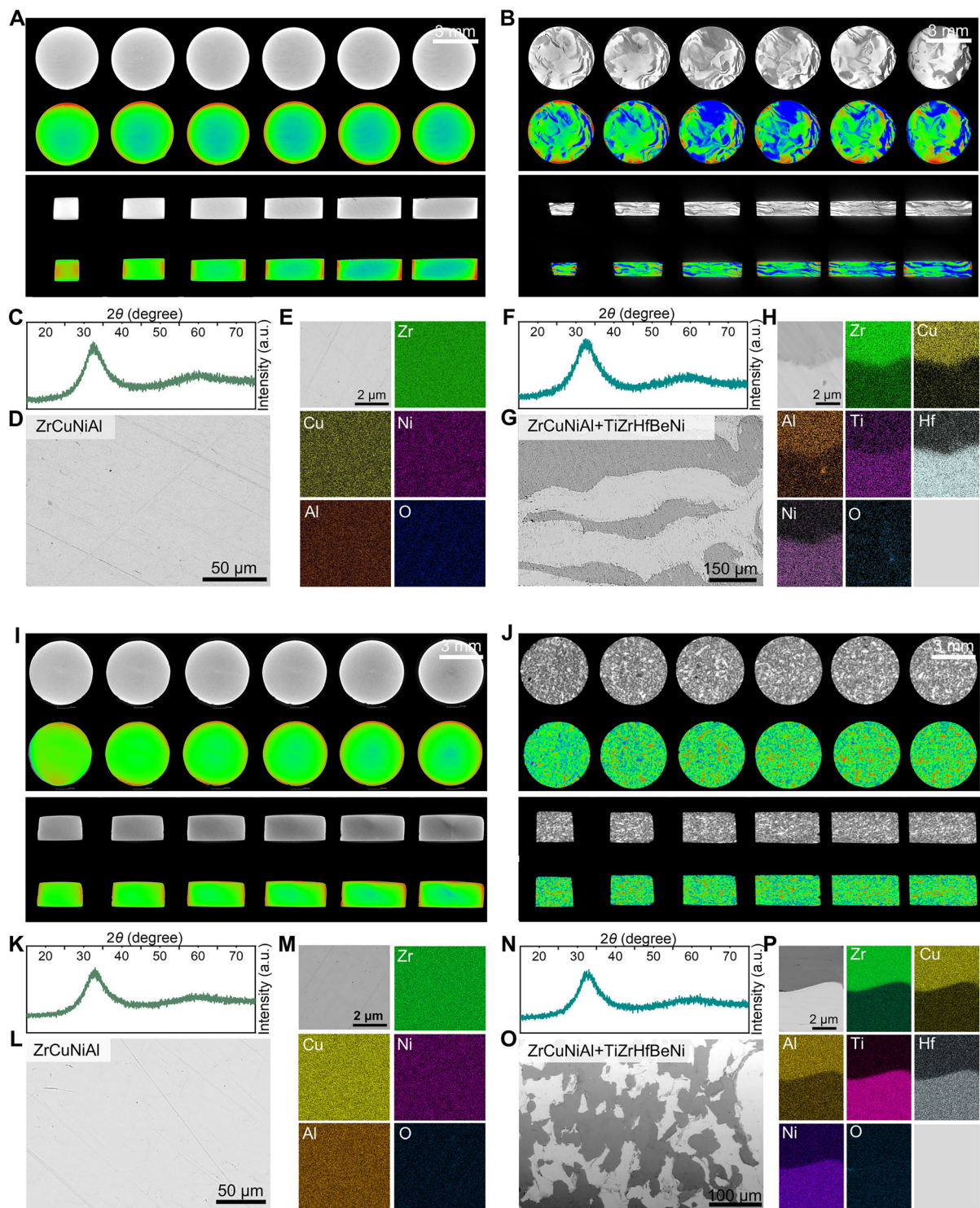


Fig. 3 Bonding quality characterization of ribbon and powder-joined sample (underwater joining as the example). **A, B** Computed tomography (CT) scan patterns and the corresponding density distribution of homogeneous ($Zr_{55}Cu_{30}Al_{10}Ni_5$ MG) and heterogeneous ($Zr_{55}Cu_{30}Al_{10}Ni_5$ MG/ $TiZrHfBeNi$ MG) ribbon-joined samples. **C–E** XRD, field emission SEM, and corresponding EDS image of the $Zr_{55}Cu_{30}Al_{10}Ni_5$ MG ribbon-joined sample. **F–H** XRD patterns, SEM image, and corresponding EDS image of the $Zr_{55}Cu_{30}Al_{10}Ni_5$ MG/ $TiZrHfBeNi$ MG ribbon-joined sample. **I, J** CT scan patterns and the corresponding density distribution of homogeneous ($Zr_{55}Cu_{30}Al_{10}Ni_5$ MG) and heterogeneous ($Zr_{55}Cu_{30}Al_{10}Ni_5$ MG/ $TiZrHfBeNi$ MG) powder-joined samples. **K–M** XRD patterns, SEM image, and corresponding EDS image of the $Zr_{55}Cu_{30}Al_{10}Ni_5$ MG powder-joined sample. **N–P** XRD patterns, SEM image, and corresponding EDS image of the $Zr_{55}Cu_{30}Al_{10}Ni_5$ MG/ $TiZrHfBeNi$ MG powder-joined sample

based powder) demonstrate a seamless joint (Fig. 3K–M) without detectable oxide residues at the interface (Fig. 3M). Distinct phenomena emerge in heterogeneous systems (Fig. 3O, P): Zr55/TiZrHfBeNi composites exhibit simultaneous softening of both constituents prior to interfacial merging, with neither material retaining the original spherical powder morphology; instead, they form an interpenetrated microstructure. These differential bonding patterns originate from ultrasonic softening kinetics – a comparable softening behavior during vibrational energy dissipation in TiZrHfBeNi MG and Zr₅₅Cu₃₀Al₁₀Ni₅ MG.

3.3 Joining mechanism

Transmission electron microscopy (TEM) characterization was employed to analyze the interfacial bonding mechanisms of MGs thoroughly. Taking the example of the joining between Zr₅₅Cu₃₀Al₁₀Ni₅ MG and TiZrHfBeNi MG, as illustrated in Fig. 4, different bonding behaviors were observed among bulk-, ribbon-, and powder-joined samples. For bulk MGs, the intense interface mixing was pretty pronounced under TEM observation, leading to a homogeneous layered structure of two distinct amorphous phases at the nanoscale (Fig. 4A, B). Notably, significant elemental diffusion occurred at the interface of two phases due to the vigorous mixing of softened MG (Fig. 4C, D), resulting in the formation of new compositional phases within the amorphous matrix. High-resolution imaging and diffraction patterns confirmed the amorphous nature of both phases and the intensely mixed region (Fig. 4E). In contrast, for ribbon-joined samples, interface mixing effects were also observed but only exist at a smaller scale, localized near the interface compared to bulk-joined samples (Fig. 4F–G). Meanwhile, the diffusion layer between the two amorphous phases in ribbon-joined samples showed relatively thin, ~ 20 nm (Fig. 4H–I), maintaining an amorphous structure at the whole specimen (Fig. 4J). In powder-joined specimens, interfaces exhibited defect-free, complete bonding joints without observable interface mixing (Fig. 4K–L), possibly due to insufficient viscosity reduction of MG during the powder bonding process. The diffusion performance resembled that of ribbon-joined samples, showing thin diffusion layers (10–20 nm) (Fig. 4M) while maintaining an amorphous structure (Fig. 4N).

The joining process in special environments has been experimentally verified to exhibit no excessive temperature increase, as depicted in Fig. 1D. This finding implies the existence of a distinct joining mechanism that is not reliant on temperature elevation. The previous series of characterization results (Figs. 1, 2, 3) offers evidence suggesting that all the joining phenomena are grounded in the softening flow of MGs. In a series of previous works, we

referred to it as ultrasonic vibration-induced plasticity (UVIP) [36], which defines the softening behavior of amorphous alloys under ultrasonic vibration. The question then arises: What is the mechanism of this process?

It is well-established that bulk MGs exhibit structural heterogeneity due to their liquid-like and solid-like regions [53]. The solid-like regions in these materials form a network structure that acts as a scaffold for elastic deformation, while the liquid-like regions, embedded within this network, serve as viscoelastic flow units capable of energy dissipation during deformation processes [54]. Under localized shear loading, these liquid-like regions have demonstrated the ability to absorb significant amounts of energy, leading to their expansion and growth [55, 56]. Notably, the UVJ process generates high-frequency vibrational loading. Drawing insights from structurally analogous saturated soil models with inherent heterogeneity [57], studies have indicated that under high-frequency cyclic loading, high pressures are prone to accumulate in the liquid-like regions. This is because there is insufficient time for stress relaxation, leading to a continuous increase in pressure within these regions [57]. When subjected to ultrasonic vibration with frequencies exceeding 20,000 Hz, the liquid-like regions in MGs undergo rapid expansion and propagate toward the solid-like network within a very short time frame (Fig. 5A) [47]. Once a critical number of these liquid-like regions have accumulated and interconnected, the elastic network structure is disrupted, leading to the material's transition to a viscous, softening behavior (Fig. 5A).

To elucidate the mechanism of UVIP, dynamic scanning probe microscopy (DSPM) was employed to systematically analyze the viscoelastic loss tangent ($\tan\delta$) of Zr-based MGs. In this context, δ represents the phase shift between the dynamic force and amplitude, and detailed experimental protocols are provided in the Methods section. The obtained results closely resemble those from traditional dynamic mechanical analysis (DMA), underscoring the validity of our approach. As depicted in Fig. 5B–D, the viscoelastic loss tangent maps at probe frequencies of 200, 72,000, and 142,000 Hz reveal distinct patterns in the Zr-based MGs. Statistical analysis of these data, presented in Fig. 5E, demonstrates that at a frequency of 200 Hz, the dynamic heterogeneity of MGs is most pronounced, with $\tan\delta$ exhibiting a perfect Gaussian distribution. At 72,000 Hz, the overall $\tan\delta$ value significantly increases to an average of 0.27, while dynamic heterogeneity remains observable. Notably, when the probe frequency is raised to 142,000 Hz, all $\tan\delta$ values in the scanned area are consistently around 0.28, indicating that the atoms in this region are highly activated and fully transformed into a liquid-like state. Furthermore, comparative experiments conducted on crystallized Zr-based MGs at 142,000 Hz

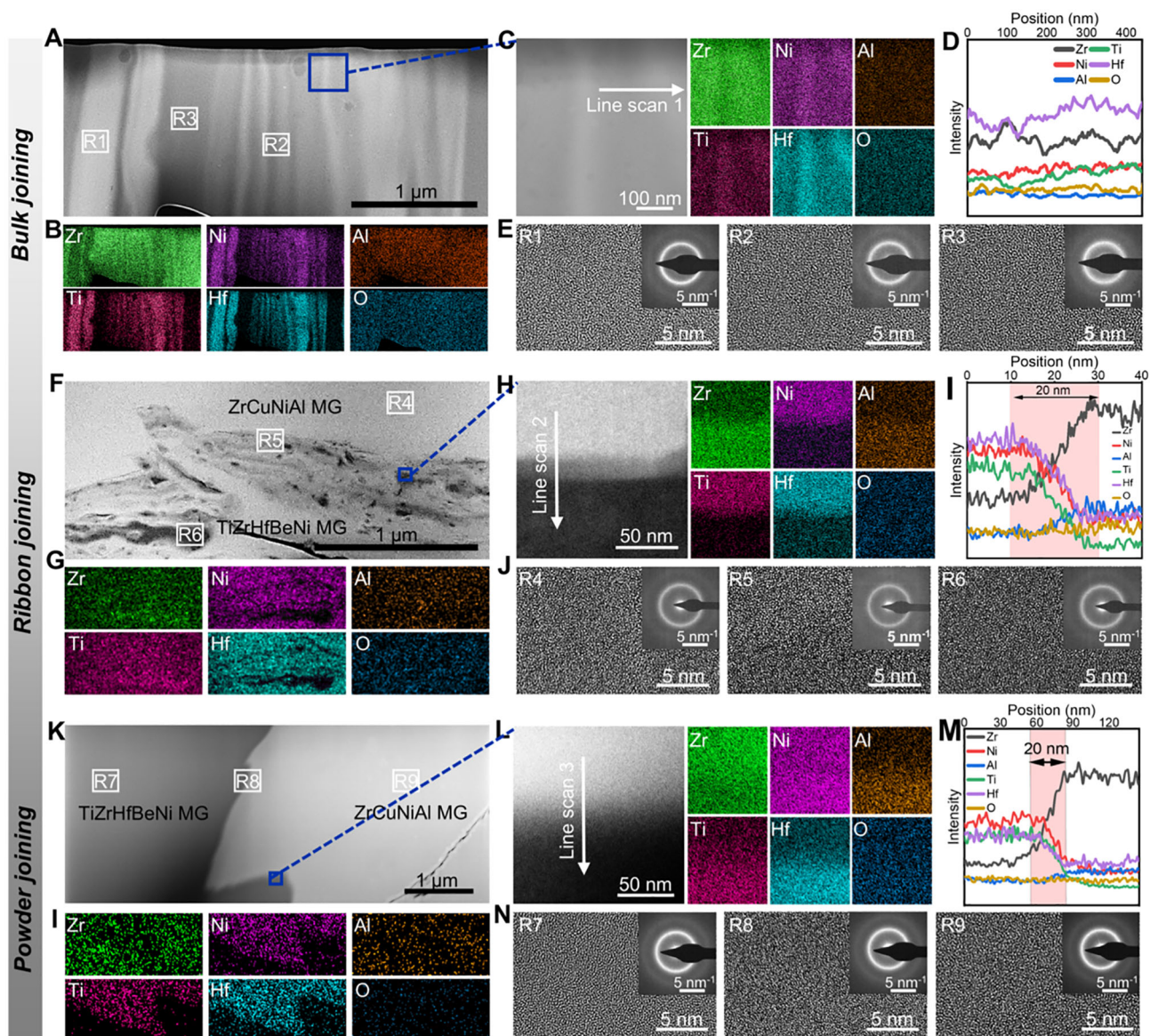


Fig. 4 TEM interface observations of joined samples of bulks, ribbons, and powders (underwater joining as the example). **A, B** HAADF image at the interface of the heterogeneous joined ($Zr_{55}Cu_{30}Al_{10}Ni_5$ MG/ $TiZrHfBeNi$ MG) sample of bulk and the corresponding EDS mapping. **C** HAADF and corresponding EDS mapping at the microscopic interface region of in a. **D** EDS line scan through the joined interface. The scanning direction is shown in C. **E** High-resolution image and SAED patterns corresponding to the R1, R2, and R3 regions in A. **F–J** Comprehensive characterization of ribbon-joined samples via TEM and EDS, similar to A–E. **K–N** Comprehensive characterization of powder-joined samples via TEM and EDS, similar to A–E

revealed no significant increase in $\tan\delta$ (Fig. S7), confirming that the elevated $\tan\delta$ observed under high-frequency vibration is a unique characteristic of the amorphous state. This finding underscores the distinct viscoelastic behavior of MGs in their non-crystalline form under high-frequency excitation.

Meanwhile, to provide a more intuitive understanding of the high-frequency loading effects on MG softening, $\tan\delta$ was utilized to estimate changes in viscosity [42]. By employing a simplified Maxwell model [42, 58], the

relationship between relaxation time (τ) and $\tan\delta$ can be derived as:

$$\tau = 1/(\omega \tan \delta) \quad (1)$$

where ω represents the angular frequency of the sinusoidal variation. Experimental evidence has established that relaxation time and viscosity are directly proportional in such viscoelastic systems [59]. Therefore, through model simplification, we obtain comparative data for viscosity (or relaxation time) at different frequencies, as shown in

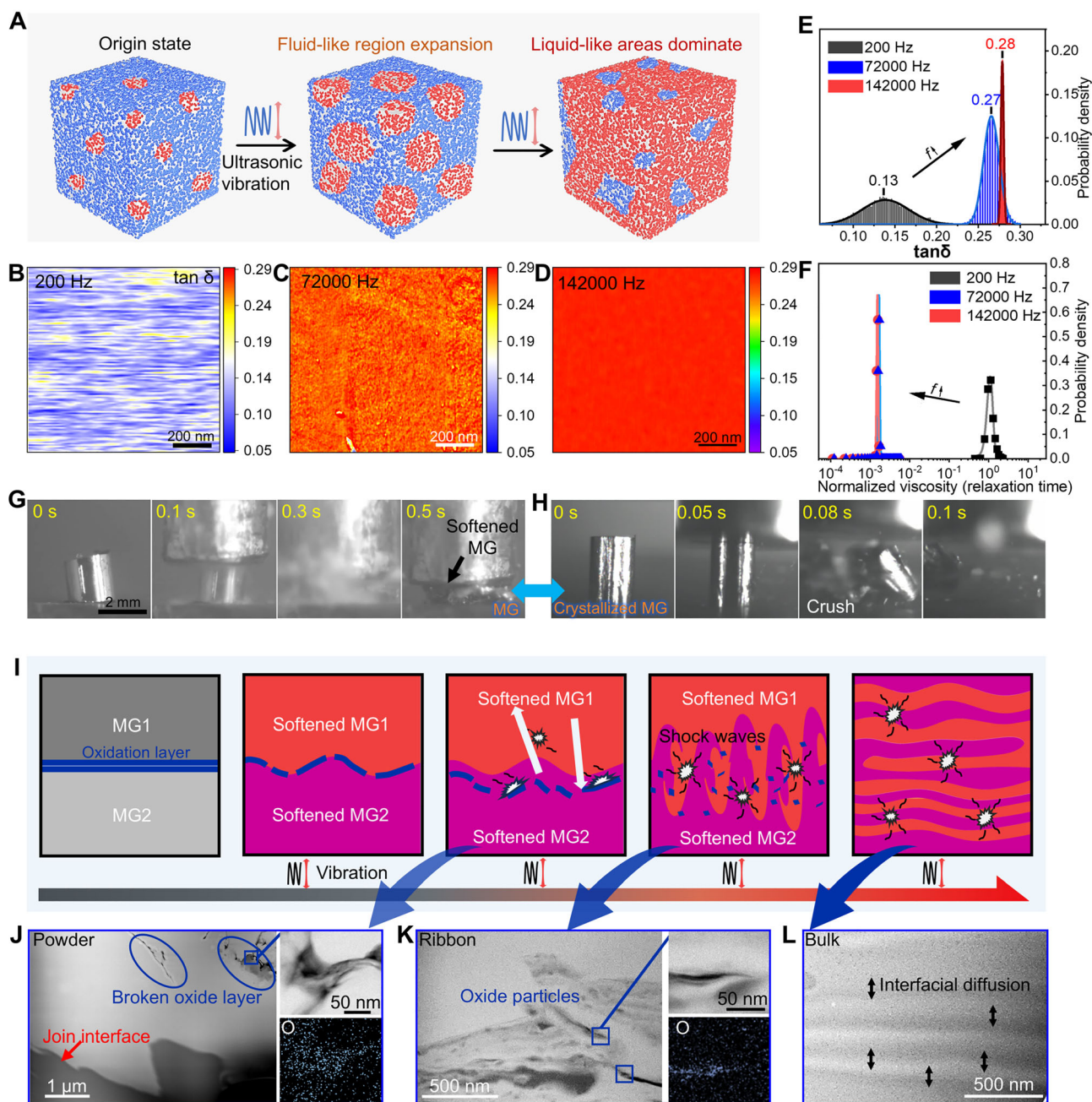


Fig. 5 Joining mechanisms. **A** Schematic diagram of ultrasonic vibration-induced plasticity (UVIP) of MG (atomic scale). **B–D** Viscoelastic loss tangent map at $f = 200$, 72,000, and 142,000 Hz. **E** Statistical analysis of b and c with a good fit of Gaussian distribution. **F** Viscosity (or relaxation time) distribution after normalizing the value of the peak position at $f = 200$ Hz. **G** Softening process of $Zr_{55}Cu_{30}Al_{10}Ni_5$ MG captured by a high-speed camera. **H** Crushing process of crystallized $Zr_{55}Cu_{30}Al_{10}Ni_5$ MG captured by a high-speed camera. **I** Schematic diagram of the mechanism of the ultrasonic vibration joining (UVJ) process, illustrating the changes in the joint interface and the oxide layer. **J, K** Interface image and oxide layer distribution of the heterogeneous ($Zr_{55}Cu_{30}Al_{10}Ni_5$ MG/ $TiZrHfBeNi$ MG) powder and ribbon-joined specimen, with an enlarged view of the local oxide layer and O element distribution spectrum shown in the right inset. **L** Interface image of the bulk heterogeneous ($Zr_{55}Cu_{30}Al_{10}Ni_5$ MG/ $TiZrHfBeNi$ MG) joined specimen

Fig. 5F. By normalizing the peak position of viscosity (or relaxation time) at $f = 200$ Hz, it is evident that as the frequency increases from 200 to 142,000 Hz, the viscosity (or relaxation time) of the MG decreases by three orders of

magnitude. The rapid softening of a single $Zr_{55}Cu_{30}Al_{10}Ni_5$ MG under ultrasonic vibration in a confined underwater environment with limited temperature rise (Fig. 5G) provides direct evidence of this unique

mechanism, as detailed in Movie S2. In contrast, the crystallized $Zr_{55}Cu_{30}Al_{10}Ni_5$ MG exhibits rapid brittle fracture rather than softening under ultrasonic vibration (Fig. 5H) [60], as detailed in Movie S3.

The mechanism and process of UVJ can be clarified through the series of characterizations described above. According to existing evidence, ultrasonic vibration exerts two effects on MG (Fig. 5I). Firstly, the established process of softening MGs into a fluid state is the foundation of the joining of MGs. Secondly, acoustic streaming and cavitation effects are typical in classical viscoelastic fluids, where vibrational waves attenuate during propagation, leading to these two effects (Fig. 5I) [61]. Specifically, acoustic streaming exhibits a quadratic nonlinearity with the ultrasound velocity, akin to the Navier–Stokes relationship [62], while cavitation phenomena occur during the nonlinear oscillation and collapse of bubbles [63]. The above nonlinear effects promote the movement of liquid materials in different directions and ultimately impact the samples.

Under sufficient energy input, the MG near the interface undergoes significant softening and transitions into a liquid state. Upon further application of high-intensity ultrasonic vibrations, pronounced cavitation and acoustic streaming effects are induced (Fig. 5I), which generate high-intensity shock waves and strong convection currents within the fluid. These effects primarily accumulate at the solid–liquid interface, leading to the gradual distortion of the MG interface. The brittle oxide layers at the interface are vibrated and partially fractured, creating gaps through which the fluid MG can spill and establish full contact with the liquid or solid phase. Leveraging the high atomic migration rate inherent to liquid MG [42], metallurgical bonding is rapidly established, forming a diffusion layer with substantial depth. Subsequently, the brittle oxide layer is fractured into nanoparticles dispersed throughout the matrix material under the influence of ultrasonic vibration. Simultaneously, the two MG phases at the interface undergo thorough mixing, forming nano to microscale mixing regions (Fig. 5I). With the sustained application of ultrasonic vibration, the mixing effect becomes increasingly pronounced and extensive, and meanwhile facilitates significant element interdiffusion between the two phases (Fig. 5I).

Due to substantial disparities in the area of the joining surface, the three morphologies of raw materials—bulks, ribbons, and powders—display distinct joining interfaces. The powders joining are characterized by an abundance of surfaces and voids, which increase the number of media for ultrasonic vibration propagation and then attenuate the transmission. As a result, the joined interface in powder remains in the earlier stage. As illustrated in Fig. 5J, relatively smooth bonding interfaces and fractured gaps

between oxide layers can be observed. Conversely, the ribbon specimen (Fig. 5K) and the bulk specimen (Fig. 5L) experience more intense MG softening and cavitation effects. This is attributed to the more direct vibration interaction with the bonding interface.

3.4 Mechanical performance

A systematic investigation was conducted to evaluate the mechanical characteristics of joined specimens with distinct morphological features. Microhardness analysis revealed that both bulk-joined and ribbon-joined samples exhibited Vickers hardness (HV) values comparable to as-cast bulk samples (Fig. 6A). In contrast, powder-joined specimens demonstrated a 5.8% hardness enhancement, reaching an average of 546.5 HV, potentially linked to their modified atomic configurations. Nanoindentation characterization further corroborated these trends, showing minimal deviations in elastic modulus across all specimen types—ribbon and powder samples displayed moduli of 103.68 and 102.68 GPa, respectively, aligning closely with as-cast reference values (Fig. 6B, C). Notably, the powder-joined specimens exhibited superior nanohardness at 6.97 GPa, exceeding other configurations by approximately 0.6 GPa. This enhancement can be rationalized by the extended ultrasonic treatment duration during the joining process, which introduced intensified energy input to promote structural densification through free volume annihilation and atomic rearrangement [64] in the powder-joined specimens.

Compression experiments were also conducted on the as-cast Zr-based MG, ribbon-joined sample, and powder-joined sample (Fig. 6D). The experimental results show that the compression strength of the ribbon sample was 1805 MPa, which is $\sim 94.4\%$ of that of the as-cast sample. In contrast, the powder-joined sample exhibited a higher compression strength of 1904 MPa, nearly identical to that of the as-cast sample (99.6%). Critically, both joined samples demonstrated compressive properties comparable to those welded in ambient atmospheric conditions (Fig. S8), confirming their environmental adaptability. Fracture morphology reflects the deformation characteristics during the material's failure process, so fracture images of the as-cast MG (Fig. 6E), ribbon-joined sample (Fig. 6F), and powder-joined sample (Fig. 6G) are presented. Overall, the fracture surfaces of all samples exhibited oblique shear cracks, indicating classic shear fracture behavior. The fracture surface of the as-cast sample displayed the typical uniform dimple-like pattern with a size of about 30–50 μm . In contrast, the fracture morphology of the powder sample revealed differences: the dimple size (1–5 μm) was much smaller than that in the as-cast MG material, with these fine dimple-like patterns

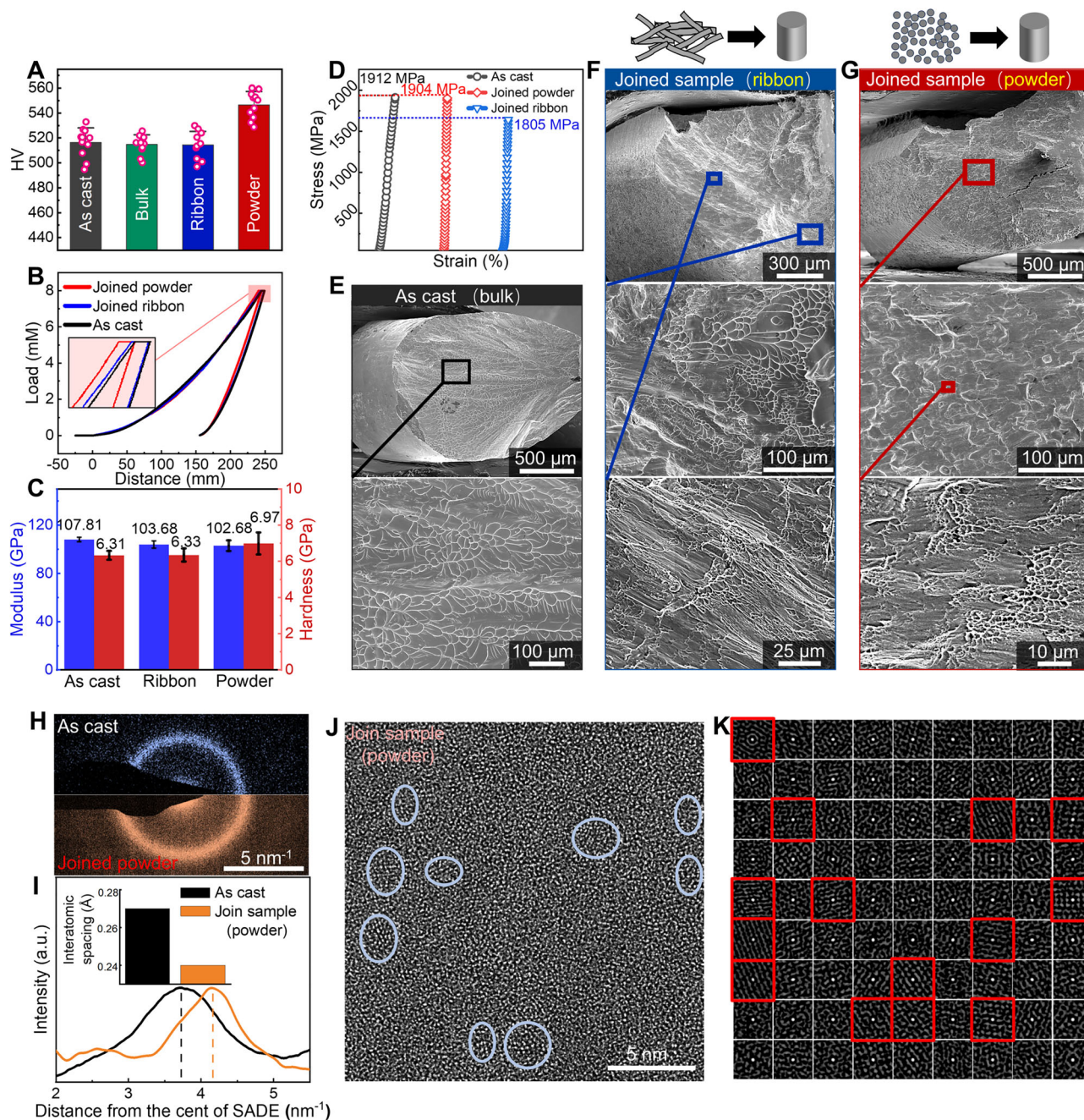


Fig. 6 Mechanical performance of joined MGs. **A** Microhardness test results on the surface of the samples (the joined samples of bulk, ribbon, and powder). **B** Load displacement curve for as-cast $Zr_{55}Cu_{30}Al_{10}Ni_5$ MG and various joined samples. **C** Comparison of the hardness and modulus between the as-cast MG, ribbon-joined sample, and powder-joined sample. The error bars represent the standard deviations of the measured values ($n = 10$). **D** Stress–strain curves of $Zr_{55}Cu_{30}Al_{10}Ni_5$ MG under compressive testing, including the as-cast MG, ribbon-joined samples, and powder-joined samples. Cross-sectional morphology images: **E** as-cast MG, **F** ribbon-joined sample, and **G** powder-joined sample. **H** SADE pattern of the as-cast MG and powder-joined sample. **I** Electron diffraction intensity profiles extracted from SADEs. The inset shows the corresponding average interatomic spacing. **J** HRTEM images of $Zr_{55}Cu_{30}Al_{10}Ni_5$ powder-joined sample. **K** Autocorrelation maps (consisting of 81 small segments) of J, respectively. Each segment has a size of 1.995×1.995 nm

concentrated in some individual units. And for the ribbon-joined sample, it exhibited both large and small dimple-like patterns in the fracture regions.

The as-cast MG demonstrates distinct free volume enriched domains, which serve as preferred sites for the unrestricted propagation of shear bands during plastic

deformation [27]. This characteristic is prominently reflected in the fracture morphology, where uniformly distributed large-scale dimples ($\sim 50 \mu\text{m}$) are observed. In contrast, powder-joined samples retain macroscopically defect-free amorphous structures through advanced UVJ. However, a few sub-surface defects, such as nanoscale pores and oxide layer residues, persist at interfacial regions (Fig. 5J). These microstructural imperfections elevate local stress concentration and reduce the energy barrier for crack nucleation [65], leading to fracture surfaces dominated by small-sized dimples.

Structural characterization further reveals that the powder-joined samples attain a moderately relaxed state during processing, as confirmed by HRTEM images of as-cast and powder-joined specimens (Fig. 6J). Both MGs exhibit characteristic amorphous features with long-range atomic disorder, supported by corresponding selected-area electron diffraction (SAED) patterns (Fig. 6H). This relaxed state manifests as an 11.2% increase in average interatomic relative to the as-cast counterpart (Fig. 6I). Beyond structural relaxation, the evolution of local ordering provides an alternative pathway to modulate free volume distribution in the glassy matrix [66, 67]. Quantitative analysis via the auto-correlation function (ACF) method applied to HRTEM images reveals enhanced atomic order in selected sub-regions (highlighted by red rectangles in Figs. 6K and S9), indicating progressively intensified local ordering with extended processing time and energy (Fig. 1C). The above microstructural evolution effectively impedes the unrestricted propagation of shear bands. The confined shear bands undergo compelled repeated nucleation among multiple obstacles, generating a densely distributed, nanoscale shear band network that directly correlates with refined dimple morphology during fracture [68, 69]. Experimental validation confirms that such structural optimization enhances fracture strength in Zr-based MGs by approximately 10% [70], consistent with the observed superior mechanical performance in powder samples. The counterbalancing effects of more stable structural states and defect-induced stress concentration ultimately lead to comparable bulk fracture strength between powder-joined and as-cast specimens.

4 Conclusion

This study pioneers a strategy for joining MGs with different forms in extreme environments, enabled by the unique combination of ultrasonic-induced rapid room-temperature MG softening and hydrodynamic mixing of liquid-like MG. The developed technology demonstrates three groundbreaking advantages: (1) form-independent bonding compatibility across bulk, ribbon, and powder configurations; (2) environmental versatility addressing

polar, subaquatic, and aerospace operational constraints; and (3) mechanical integrity preservation with $> 95\%$ base material strength retention. This work provides transformative solutions for offshore, polar, and space applications.

Acknowledgements The work was financially supported by the Science and Technology Innovation Commission Shenzhen (Nos. RCJC20221008092730037 and 20220804091920001), the Key-Area Research and Development Program of Guangdong Province (No. 2024B0101070001), the Research Team Cultivation Program of Shenzhen University (No. 2023QNT001), and the National Natural Science Foundation of China (Nos. 52071078 and 52201186). We thank the Instrumental Analysis Center of Shenzhen University for the assistance with the electron microscope.

Author contributions Lu-Yao Li was contributed writing–review and editing, writing–original draft, validation, methodology, investigation, formal analysis, data curation, and conceptualization. Jian-Yu Chen was involved in methodology and data curation. Li-Xing Zhu, Yu Zhang, Jian Zhu, and Xing-Ran Zhao were performed validation and data curation. Xin Li was done validation, methodology, and data curation. Wei Li and Kang-Yu Lin did data curation. Xiao-Di Liu was carried out supervision and data curation. Chen-Chen Yuan was attributed supervision, formal analysis, and writing–review and editing. Jiang Ma was responsible for writing–review and editing, validation, supervision, resources, project administration, investigation, funding acquisition, and formal analysis.

Declarations

Conflict of interests The authors declare that they have no conflict of interest.

Data availability All data needed to evaluate the conclusions in the paper are present in the paper and/or the supplementary information. Data are also available from the corresponding author upon request.

References

- Nicholas MG. Joining processes. Dordrecht: Kluwer Academic Publishers; 1998.
- Brandon D, Kaplan WD. Joining processes: an introduction. Chichester: Wiley; 1997.
- Weman K. Welding processes handbook. Cambridge: Woodhead Publishing; 2003.
- Angelo P, Subramanian R, Ravisankar B. Powder metallurgy: science, technology and applications. Delhi: PHI Learning Pvt Ltd; 2022.
- Fang ZZ, Paramore JD, Sun P, Chandran KSR, Zhang Y, Xia Y, Cao F, Koopman M, Free M. Powder metallurgy of titanium—past, present, and future. *Int Mater Rev.* 2018;63(7): 407–59. <https://doi.org/10.1080/09506608.2017.13660>.
- Shahrubudin N, Lee TC, Ramlan R. An overview on 3D printing technology: technological, materials, and applications. *Procedia Manuf.* 2019;35:1286–96. <https://doi.org/10.1016/j.promfg.2019.06.089>.
- Tan HW, Tran T, Chua CK. A review of printed passive electronic components through fully additive manufacturing methods. *Vir Phys Prototyping.* 2016;11:271–88. <https://doi.org/10.1080/17452759.2016.1217586>.
- Łabanowski J, Fydrych D, Rogalski G. Underwater welding—a review. *Adv Mater Sci.* 2008;8:11–22. <https://doi.org/10.2478/v10077-008-0040-3>.

9. Sun GF, Wang ZD, Lu Y, Chen MZ, Yang K, Ni ZH. Underwater laser welding/cladding for high-performance repair of marine metal materials: a review. *CJME*. 2022;35:5. <https://doi.org/10.1186/s10033-021-00674-0>.
10. Sharma SK, Maheshwari S. A review on welding of high strength oil and gas pipeline steels. *J Nat Gas Sci Eng*. 2017;38:203–17. <https://doi.org/10.1016/j.jngse.2016.12.039>.
11. Mahdi E, Eltai E. Development of cost-effective composite repair system for oil/gas pipelines. *Compos Struct*. 2018;202:802–6. <https://doi.org/10.1016/j.compstruct.2018.04.025>.
12. Thirsk R, Kuipers A, Mukai C, Williams D. The space-flight environment: the International Space Station and beyond. *CMAJ*. 2009;180(12):1216–20. <https://doi.org/10.1503/cmaj.081125>.
13. Ingersoll AP, Svitek T, Murray BC. Stability of polar frosts in spherical bowl-shaped craters on the moon, Mercury, and Mars. *Icarus*. 1992;100(1):40–7. [https://doi.org/10.1016/0019-1035\(92\)90016-Z](https://doi.org/10.1016/0019-1035(92)90016-Z).
14. Zhang L-C, Jia Z, Lyu F, Liang S-X, Lu J. A review of catalytic performance of metallic glasses in wastewater treatment: recent progress and prospects. *Process Saf Environ Prot*. 2019;105:100576. <https://doi.org/10.1016/j.psep.2018.12.006>.
15. Di X, Ji S, Cheng F, Wang D, Cao J. Effect of cooling rate on microstructure, inclusions and mechanical properties of weld metal in simulated local dry underwater welding. *Mater Des*. 2015;88:505–13. <https://doi.org/10.1016/j.matdes.2015.09.025>.
16. Rowe M, Liu S. Recent developments in underwater wet welding. *Sci Technol Weld Join*. 2001;6(6):387–96. <https://doi.org/10.1179/stw.2001.6.6.387>.
17. Kielczynski W, Lesinski K, Piatkowski T. Technologies and equipment for underwater welding and cutting. *Weld Int*. 1994; 8(4):257–61. <https://doi.org/10.1080/09507119409548586>.
18. Zhang X, Ashida E, Shono S, Matsuda F. Effect of shielding conditions of local dry cavity on weld quality in underwater Nd: YAG laser welding. *J Mater Process Technol*. 2006;174(1–3): 34–41. <https://doi.org/10.1016/j.jmatprotec.2004.12.009>.
19. Gooch TG. Properties of under water welds, part 2: mechanical properties. *Met Constr*. 1983;15(4):206–15.
20. Pessoa ECP, Bracarense AQ, Zica EM, Liu S, Perez-Guerrero F. Porosity variation along multipass underwater wet welds and its influence on mechanical properties. *J Mater Process Technol*. 2006;179(1–3):239–43. <https://doi.org/10.1016/j.jmatprotec.2006.03.071>.
21. Rowe MD, Liu S, Reynolds TJ. The effect of ferro-alloy additions and depth on the quality of underwater wet welds. *Weld J*. 2002;81(8):156–S.
22. Fydrych D, Rogalski G. Effect of shielded-electrode wet welding conditions on diffusion hydrogen content in deposited metal. *Weld Int*. 2011;25(03):166–71. <https://doi.org/10.1080/09507116.2010.540828>.
23. Suo H, Cheng H, Liang B, Deng K, Luo B, Zhang K, Chen H. The mechanical degradation mechanism of CFRP/Al double-lap bolted joints (with and without corrosion protections) after seawater ageing. *Compos Struct*. 2021;276:114561. <https://doi.org/10.1016/j.compstruct.2021.114561>.
24. Chen J, Ding N, Li Z, Wang W. Organic polymer materials in the space environment. *Prog Aerosp Sci*. 2016;83:37–56. <https://doi.org/10.1016/j.paerosci.2016.02.002>.
25. David SA, DebRoy T. Current issues and problems in welding science. *Science*. 1992;257(5069):497–502. <https://doi.org/10.1126/science.257.5069.497>.
26. Murphy AG, Meagher P, Norman A, Browne DJ. Mechanical and thermal stability of bulk metallic glass alloys identified as candidates for space mechanism applications. *Mater Des*. 2022;224: 111350. <https://doi.org/10.1016/j.matdes.2022.111350>.
27. Wang W-H, Dong C, Shek CH. Bulk metallic glasses. *Mater Sci Eng R Rep*. 2004;44(2–3):45–89. <https://doi.org/10.1016/j.mser.2004.03.001>.
28. Liu M, Han X, Zhao R, Lu T, Dong W, Liao C, Zhang Q, Sun Y, Dong Y, Song J. Stability of metallic glasses under simulated space conditions. *J Alloys Compd*. 2022;902:163811. <https://doi.org/10.1016/j.jallcom.2022.163811>.
29. Schuh CA, Hufnagel TC, Ramamurty U. Mechanical behavior of amorphous alloys. *Acta Mater*. 2007;55(12):4067–109. <https://doi.org/10.1016/j.actamat.2007.01.052>.
30. Wang WH. The elastic properties, elastic models and elastic perspectives of metallic glasses. *Prog Mater Sci*. 2012;57(3): 487–656. <https://doi.org/10.1016/j.pmatsci.2011.07.001>.
31. Jia Q, He W, Hua D, Zhou Q, Du Y, Ren Y, Lu Z, Wang H, Zhou F, Wang J. Effects of structure relaxation and surface oxidation on nanoscopic wear behaviors of metallic glass. *Acta Mater*. 2022;232:117934. <https://doi.org/10.1016/j.actamat.2022.117934>.
32. Wang X, Yang C, Fan C, Liu R, Sun L, Zhang J, Zhan Z, Wang W. Effect of proton irradiation on structure relaxation of $Zr_{41}Ti_{14.9}Cu_{12.6}Ni_{10.5}Be_{20.4}$ bulk metallic glass. *Chin Sci Bull*. 2004; 49:999–1001. <https://doi.org/10.1007/BF03184026>.
33. Ketov SV, Sun YH, Nachum S, Lu Z, Checchi A, Beraldin AR, Bai HY, Wang WH. Rejuvenation of metallic glasses by non-affine thermal strain. *Nature*. 2015;524(7564):200–3. <https://doi.org/10.1038/nature14674>.
34. Pang SJ, Zhang T, Asami K, Inoue A. Synthesis of Fe-Cr--Mo-C-B-P bulk metallic glasses with high corrosion resistance. *Acta Mater*. 2002;50(3):489–97. [https://doi.org/10.1016/S1359-6454\(01\)00366-4](https://doi.org/10.1016/S1359-6454(01)00366-4).
35. Johnson WL, Kaltenboeck G, Demetriou MD, Schramm JP, Liu X, Samwer K, Kim CP. Beating crystallization in glass-forming metals by millisecond heating and processing. *Science*. 2011; 332(6031):828–33. <https://doi.org/10.1126/science.1201362>.
36. Sohrabi S, Fu J, Li L, Zhang Y, Li X, Sun F, Ma J, Wang WH. Manufacturing of metallic glass components: processes, structures and properties. *Prog Mater Sci*. 2024;144:101283. <https://doi.org/10.1016/j.pmatsci.2024.101283>.
37. Inoue A, Nishiyama N, Kimura H. Preparation and thermal stability of bulk amorphous $Pd_{40}Cu_{30}Ni_{10}P_{20}$ alloy cylinder of 72 mm in diameter. *Mater Trans*. 1997;38(2):179–83. <https://doi.org/10.2320/matertrans1989.38.179>.
38. Zhou ZQ, He QF, Liu XD, Wang Q, Luan JH, Liu CT, Yang Y. Rational design of chemically complex metallic glasses by hybrid modeling guided machine learning. *npj Comput Mater*. 2021; 7(1):138. <https://doi.org/10.1038/s41524-021-00607-4>.
39. Yuan CC, Yang F, Kargl F, Holland-Moritz D, Li MZ, Wang XL, Zhang B, Wang WH, Meyer A. Sluggish dynamics in Al-containing metallic glass-forming melts. *Acta Mater*. 2025;285: 120652. <https://doi.org/10.1016/j.actamat.2024.120652>.
40. Li H, Li Z, Yang J, Ke HB, Sun B, Yuan CC, Ma J, Shen J, Wang W-H. Interface design enabled manufacture of giant metallic glasses. *Sci China Mater*. 2021;64(4):964–72. <https://doi.org/10.1007/s40843-020-1561-x>.
41. Chen W, Liu Z, Schroers J. Joining of bulk metallic glasses in air. *Acta Mater*. 2014;62:49–57. <https://doi.org/10.1016/j.actamat.2013.08.053>.
42. Ma J, Yang C, Liu X, Shang B, He Q, Li F, Wang T, Wei D, Liang X, Wu X. Fast surface dynamics enabled cold joining of metallic glasses. *Sci Adv*. 2019;5(11):eaax7256. <https://doi.org/10.1126/sciadv.aax7256>.
43. Wang G, Huang YJ, Shagiev M, Shen J. Laser welding of $Ti_{40}Zr_{25}Ni_3Cu_{12}Be_{20}$ bulk metallic glass. *Mater Sci Eng A*. 2012; 541:33–7. <https://doi.org/10.1016/j.msea.2012.01.114>.

44. Jiang MQ, Huang BM, Jiang ZJ, Lu C, Dai LH. Joining of bulk metallic glass to brass by thick-walled cylinder explosion. *Scr Mater.* 2015;97:17–20. <https://doi.org/10.1016/j.scriptamat.2014.10.027>.
45. Fujiwara K, Fukumoto S, Yokoyama Y, Nishijima M, Yamamoto A. Weldability of $Zr_{50}Cu_{30}Al_{10}Ni_{10}$ bulk glassy alloy by small-scale resistance spot welding. *Mater Sci Eng A.* 2008;498(1–2):302–7. <https://doi.org/10.1016/j.msea.2008.08.030>.
46. Wang D, Xiao BL, Ma ZY, Zhang HF. Friction stir welding of $Zr_{55}Cu_{30}Al_{10}Ni_5$ bulk metallic glass to Al–Zn–Mg–Cu alloy. *Scr Mater.* 2009;60(2):112–5. <https://doi.org/10.1016/j.scriptamat.2008.09.014>.
47. Li X, Wei D, Zhang JY, Liu XD, Li Z, Wang TY, He QF, Wang YJ, Ma J, Wang WH. Ultrasonic plasticity of metallic glass near room temperature. *Appl Mater Today.* 2020;21:100866. <https://doi.org/10.1016/j.apmt.2020.100866>.
48. Li L, Li X, Huang Z, Huang J, Liu Z, Fu J, Wen W, Zhang Y, Huang S, Ren S, Ma J. Joining of metallic glasses in liquid via ultrasonic vibrations. *Nat Commun.* 2023;14(1):6305. <https://doi.org/10.1038/s41467-023-42014-x>.
49. Li X, Liang X, Zhang Z, Ma J, Shen J. Cold joining to fabricate large size metallic glasses by the ultrasonic vibrations. *Scr Mater.* 2020;185:100–4. <https://doi.org/10.1016/j.scriptamat.2020.03.059>.
50. Li L, Li X, Huang Z, Huang J, Liu Z, Fu J, Wen W, Zhang Y, Huang S, Ren S, Ma J. Ultrasonic-assisted rapid cold welding of bulk metallic glasses. *Sci China Mater.* 2022;65(1):255–62. <https://doi.org/10.1007/s40843-021-1723-6>.
51. Maeda M, Yamasaki T, Takahashi Y, Inoue A. Interfacial microstructure and thermal stability of $Zr_{55}Cu_{30}Ni_5Al_{10}$ metallic glass joints formed by ultrasonic bonding. *Mater trans.* 2009;50(6):1263–8.
52. Leung CLA, Marussi S, Towrie M, Atwood RC, Withers PJ, Lee PD. The effect of powder oxidation on defect formation in laser additive manufacturing. *Acta Mater.* 2019;166:294–305. <https://doi.org/10.1016/j.actamat.2018.12.027>.
53. Qiao JC, Wang Q, Pelletier JM, Kato H, Casalini R, Crespo D, Pineda E, Yao Y, Yang Y. Structural heterogeneities and mechanical behavior of amorphous alloys. *Prog Mater Sci.* 2019;104:250–329. <https://doi.org/10.1016/j.pmatsci.2019.04.005>.
54. Sun F, Wang B, Luo F, Yan YQ, Ke HB, Ma J, Shen J, Wang WH. Shear punching of bulk metallic glasses under low stress. *Mater Des.* 2020;190:108595. <https://doi.org/10.1016/j.matdes.2020.108595>.
55. Wang Y-J, Jiang MQ, Tian ZL, Dai LH. Direct atomic-scale evidence for shear–dilatation correlation in metallic glasses. *Scr Mater.* 2016;112:37–41. <https://doi.org/10.1016/j.scriptamat.2015.09.005>.
56. Peng CX, Şopu D, Cheng Y, Song KK, Wang SH, Eckert J, Wang L. Deformation behavior of designed dual-phase CuZr metallic glasses. *Mater Des.* 2019;168:107662. <https://doi.org/10.1016/j.matdes.2019.107662>.
57. Galindo-Torres SA, Zhang X, Krabbenhoft K. Micromechanics of liquefaction in granular materials. *Phys Rev Appl.* 2018;10(6):064017. <https://doi.org/10.1103/PhysRevApplied.10.064017>.
58. Shiue S-T, Shen T-Y. Effect of thermal stresses on the static fatigue of double-coated optical fibers. *Mater Chem Phys.* 2005;89(1):159–63. <https://doi.org/10.1016/j.matchemphys.2004.08.030>.
59. Andrade T, Baggioli M, Pujolas O. Linear viscoelastic dynamics in holography. *Phys Rev D.* 2019;100(10):106014. <https://doi.org/10.1103/PhysRevD.100.106014>.
60. Li L, Wen W, Huang J, Fu J, Ma J. Rapid fabrication of ultra-fine grain intermetallic compound powder in milliseconds under ultrasonic vibrations. *Intermetallics.* 2022;149:107672. <https://doi.org/10.1016/j.intermet.2022.107672>.
61. Komarov SV, Kuwabara M, Abramov OV. High power ultrasonics in pyrometallurgy: current status and recent development. *ISIJ Int.* 2005;45(12):1765–82. <https://doi.org/10.2352/isijinternational.45.1765>.
62. Lighthill J. Acoustic streaming. *J Sound Vib.* 1978;61(3):391–418. https://doi.org/10.1007/978-0-387-48998-8_12.
63. Rooze J, Rebrov EV, Schouten JC, Keurentjes JTF. Dissolved gas and ultrasonic cavitation—a review. *Ultrason Sonochem.* 2013;20(1):1–11. <https://doi.org/10.1016/j.ultsonch.2012.04.013>.
64. Zhao H, Sun F, Li X, Ding Y, Yan YQ, Tong X, Ma J, Ke HB, Wang WH. Ultrastability of metallic supercooled liquid induced by vibration. *Scr Mater.* 2021;194:113606. <https://doi.org/10.1016/j.scriptamat.2020.10.048>.
65. Chen HB, Wang JF, Zhen GD, Chen SB, Lin T. Effects of initial oxide on microstructural and mechanical properties of friction stir welded AA2219 alloy. *Mater Des.* 2015;86:49–54. <https://doi.org/10.1016/j.matdes.2015.06.179>.
66. Hou L, Wang B, Liu L, Mao X, Zhang M, Yuan C, Li Z, Ju W, Feng H, Tang C. Tailoring magnetic softness of Fe-based amorphous alloys with superior magnetization by magnetic field annealing. *J Mater Sci Technol.* 2024;200:27–37. <https://doi.org/10.1016/j.jmst.2024.02.043>.
67. Li W, Wang C, Li LY, Zhang C, Ma J, Xi XK, Tao K, Qiao JC, Yuan CC, Wang WH. Manipulating defects in metallic glasses via ultrasonic treatment. *Int J Mech Sci.* 2025;287:109960. <https://doi.org/10.1016/j.ijmecsci.2025.109960>.
68. Wang WH. Correlation between relaxations and plastic deformation, and elastic model of flow in metallic glasses and glass-forming liquids. *J Appl Phys.* 2011. <https://doi.org/10.1063/1.3632972>.
69. Shi Y, Falk ML. Atomic-scale simulations of strain localization in three-dimensional model amorphous solids. *Phys Rev B.* 2006;73(21):214201. <https://doi.org/10.1103/PhysRevB.73.214201>.
70. Zhang NZ, Bian XL, Ren C, Geng C, Mu YK, Ma XD, Jia YD, Wang Q, Wang G. Manipulation of relaxation processes in a metallic glass through cryogenic treatment. *J Alloys Compd.* 2022;894:162407. <https://doi.org/10.1016/j.jallcom.2021.162407>.

Springer Nature or its licensor (e.g. a society or other partner) holds exclusive rights to this article under a publishing agreement with the author(s) or other rightsholder(s); author self-archiving of the accepted manuscript version of this article is solely governed by the terms of such publishing agreement and applicable law.